nature materials

SUPPLEMENTARY INFORMATION

DOI: 10.1038/NMAT2635

Device fabrication

Silicon nitride deposition

Silicon nitride antireflective (AR) coatings were deposited onto Si wire arrays using an Oxford Instruments Plasmalab System100 plasma-enhanced chemical vapor deposition (PECVD) tool. Silane and ammonia gas chemistry was used at 350 °C and 1 torr, and the gas ratio was adjusted to produce films with a refractive index near 2. The PECVD process was performed with in-situ stress control by alternately pulsing a 13.56-MHz radio-frequency generator and a 50-kHz low-frequency generator, both with 20 W of forward power. Due to the large surface area and aspect ratio of the arrays, the coating required a much longer deposition time than would be required for a planar film of the same thickness.

The nitride final film thickness was measured by SEM, using focused-ion beam (FIB) milling to produce wire cross-sections (Fig. S1). Individual wires were removed from the growth substrate, and deposited (horizontally) onto a Si wafer that was coated with 80 nm SiN_x (for contrast reference). This was coated with various layers of metal (Ag, Al) to facilitate milling and imaging. The deposited nitride thickness was observed to increase gradually along the length of the wires, reaching ~2x the base thickness at the top sidewall of the wire, and ~2.5x the base thickness on the top surface of the wires (Fig. S1a). Thickness appeared uniform around the diameter of the wires (Fig. S1b). The nitride thickness of the actual wire array whose absorbance is plotted in Fig. 3 was verified by milling a cross section of a single wire within the center of the array, at approx. half the height of the adjacent wires (Fig. S1c).

Multiple-angle spectroscopic ellipsometry was used to measure the optical properties of a

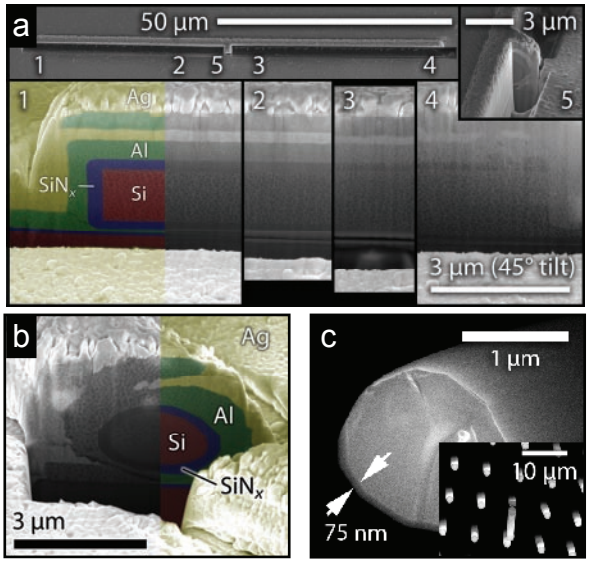

Figure S1. Determination of nitride thickness. **a,b,** cross-sectional SEM images of nitride-coated wires removed from growth substrate. Partial false-coloring added for clarity. **c,** cross-sectional SEM image of nitride-coated wire from center of wire array, with inset showing milling area.

planar film of PECVD silicon nitride. Ψ and Δ spectra, ranging from 350–2200 nm, were measured at angles of 60°, 65°, and 70°, as shown in Fig. S2a. The spectra were then fit to a Forouhi-Bloomer model for amorphous dielectric materials.[1] The real and imaginary parts of the index produced by the fit are plotted in Fig. S2b. Based on these values, the absorption of an 80-nm nitride film is negligible (<2%) throughout most of the measurement range in this study (λ > 500 nm).

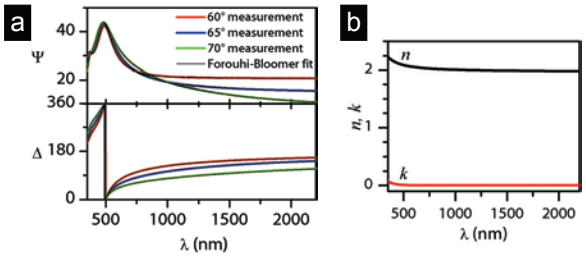

Figure S2. Spectroscopic ellipsometry characterization of silicon nitride film.

DOI: 10.1038/NMAT2635

Al_2O_3 light-scattering particles

Alumina particles were embedded within the PDMS infill of selected wire arrays, to scatter the light that might otherwise pass between the wires without being absorbed. Al_2O_3 particles (< 0.9 μm nominal particle size) were hydrophobicized via surface functionalization (> 1 hr in 10 μl/ml trimethylchlorosilane in CH_2CL_2). After washing several times to removed excess trimethylchlorosilane, the particles were suspended in CH_2CL_2 by sonication. This suspension was mixed with uncured PDMS to yield a ratio of 1:10:10 Al2O3:CH2Cl2:PDMS by weight. The suspension was drop cast onto the wire arrays and spun at speeds of 1500–3000 RPM (depending on device area). Prior to curing, the arrays were centrifuged for several minutes to drive the Al_2O_3 particles towards the bottom of the PDMS layer. Wire array films were cured and peeled-off as described in the *Methods* section.

Following characterization of the optical absorption, a wire array with the SiN_x AR-coating and embedded Al_2O_3 particles was sliced in half with a razor blade for cross-sectional imaging. Due to the insulating nature of the PDMS, an environmental SEM was employed, using H_2O vapor at 2–4 mbar to mitigate charging effects. Fig. S3a shows the cross-section of the wire array whose absorption is plotted in Fig. 3. Alumina particles were observed between the wires, distributed within the lower half of the PDMS film. Near the edge of this specimen, larger agglomerates of alumina particles were also observed above the top of the wire array (Fig. S3b), although these areas were not illuminated during optical measurements. Some wires were inadvertently severed during the cross-sectioning process, allowing the ~80 nm SiN_x AR-coating to be observed (Fig. S3b, inset).

The optical properties of the PDMS-embedded Al_2O_3 particles were also measured, to ensure that they did not contribute to parasitic absorption within the Si wire arrays. A drop of the PDMS with suspended Al_2O_3 particles was cured on a quartz slide without spinning or centrifuging, to yield a film thickness comparable to that of the wire arrays (est. 300 μm). The absorption of this film is shown in Fig. S4, indicating absorption was less than 2% throughout the spectral range of this study.

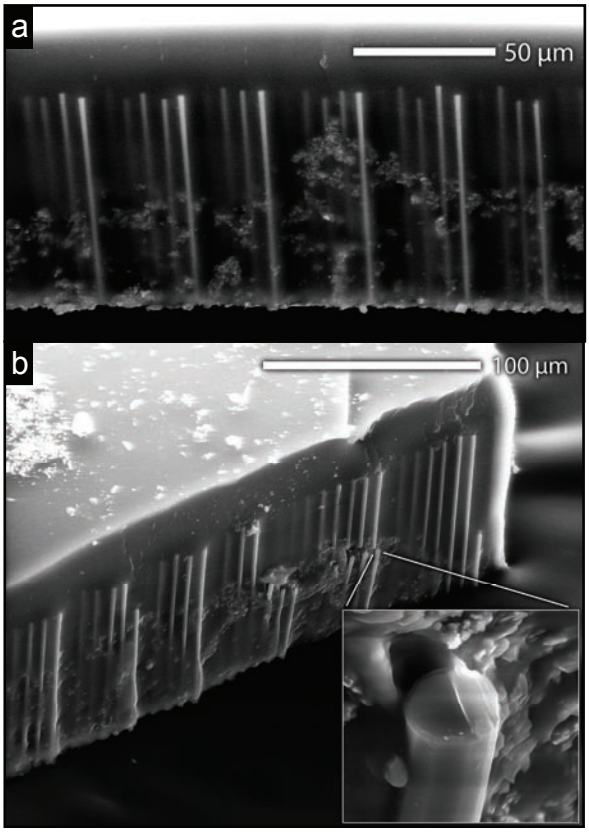

Figure S3. SEM images of the polymer-embedded Si wire array that was measured in Fig. 3. **a,** cross-section of central area of array showing distribution of Al_2O_3 particles. **b,** view of edge of array, with inset showing the ~80 nm SiN_x AR-coating visible on wire sidewall.

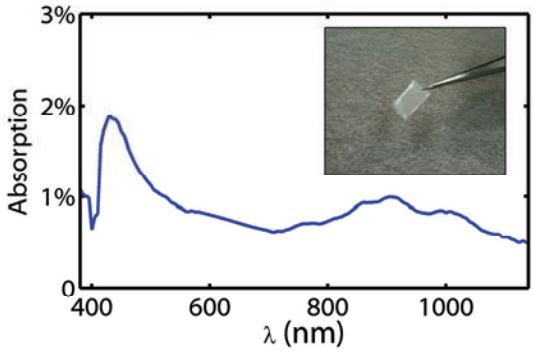

Figure S4. Integrated normal-incidence absorption of ~300 μm-thick film of Al_2O_3 particles embedded within PDMS. Inset: Digital photograph of this specimen.

Integrating sphere measurements

Experimental apparatus

Integrated reflection and transmission measurements were performed with a custom-built 4" integrating sphere apparatus, as shown in Figure S5. The internal surfaces of the sphere, baffles, port apertures, and stages were sandblasted, then cleaned and coated with a $BaSO_4$ integrating sphere coating (LabSphere, Inc) to achieve nearly ideal Lambertian reflectivity. Illumination was provided by a chopped supercontinuum laser source (Fianium) coupled to a 0.25 m monochromator, allowing tunable excitation from 400 nm to > 1600 nm with a typical passband of < 0.5 nm. The illumination beam was focused to produce a 1 mm spot size (FWHM) with < 0.1° of beam divergence. A pair of calibrated Si (400–1150 nm) or Ge (1000–1600 nm) photodiodes was used to simultaneously monitor the light intensity of the incident beam (referenced via a quartz beam-splitter) and the light intensity internal to the sphere. Measurements were typically performed from 400–1150 nm in 2 nm increments, except between 1058 and 1070 nm where the reported values were interpolated from measurements at either endpoint due to an unstable peak in the illumination intensity at 1064 nm.

In transmission mode, each specimen was placed over a 10 mm-diameter entrance port of the integrating sphere (Fig. S5a). Motorized operation permitted eucentric rotation and translation in two dimensions with 0.1° and 100 μm resolution, respectively. The wire array transmission was normalized to the previously measured transmission of the quartz slides which was accessed by motorized translation of the sphere at the beginning of the measurement sequence. In reflection mode, each specimen was placed at the center of the sphere over a 5 mm-diameter light trap that absorbed any light transmitted through the specimen (Fig. S5b). Motorized operation permitted eucentric rotation in one dimension (θ_x) with 0.1° resolution. The tilt in the second (θ_y) dimension was typically fixed at ~0.5°, to prevent the specular reflection from escaping the sphere through the 1 mm-diameter illumination port aperture. The wire array reflection was normalized to a

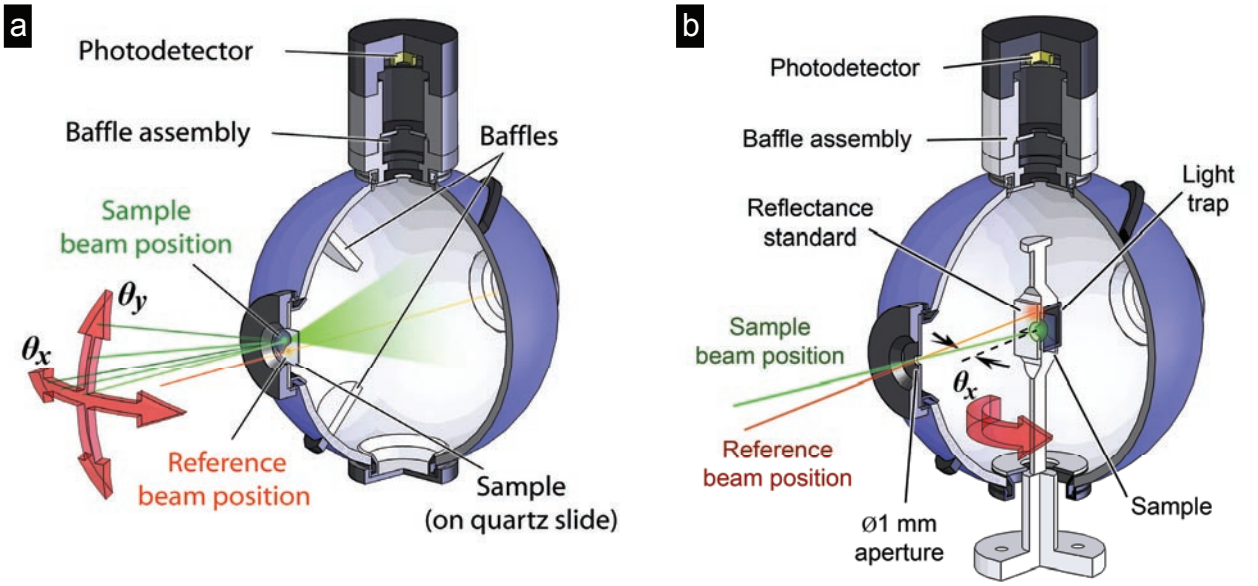

Figure S5. Illustration of integrating sphere measurements. **a,** configuration for transmission measurements. The incidence beam angle variation was achieved by the eucentric tilt of the entire sphere apparatus. **b,** configuration for reflection measurements. The incidence beam angle variation was achieved by rotation of the reflection stage within the sphere.

DOI: 10.1038/NMAT2635

reflectance standard (LabSphere, Inc) within the sphere, which was accessed by motorized translation and rotation of the specimen stage and sphere assembly. For the measurements performed on specular back-reflectors, each wire array film was removed from the transparent quartz slide and placed onto a slide which had been coated with >100 nm of evaporated Ag. For the Lambertian back reflector studies, each wire array film was removed from the transparent quartz slide and placed onto a sheet of Al, that had been cleaned, roughened, and coated with $BaSO_4$ like the other internal surfaces of the integrating sphere. The reflectivity of such surfaces exceeded 97% throughout most of the measurement range (see Fig. S6).

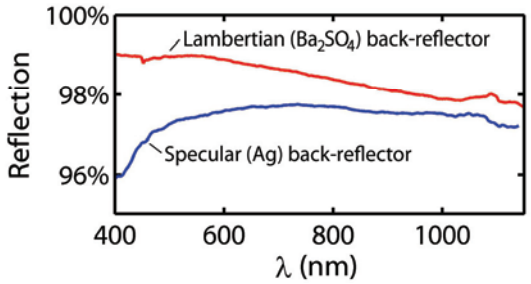

Figure S6. Integrated reflection measurements of the back-reflectors used in these studies.

Determination of absorption

The absorption of each specimen was determined from the wavelength- and angle-resolved integrated transmission and reflection measurements. For non-opaque specimens (e.g. wire arrays placed upon quartz slides), absorption was calculated as:

$$A(\lambda,\theta) = 1 - R(\lambda,\theta) - T(\lambda,\theta) \quad (1)$$

For opaque specimens (e.g. the commercial Si solar cell) or those placed on opaque back-reflectors, absorption was calculated from reflectivity measurements only:

$$A(\lambda,\theta) = 1 - R(\lambda,\theta) \quad (2)$$

Example transmission, reflection, and resulting absorption measurements of a triangular-tiled

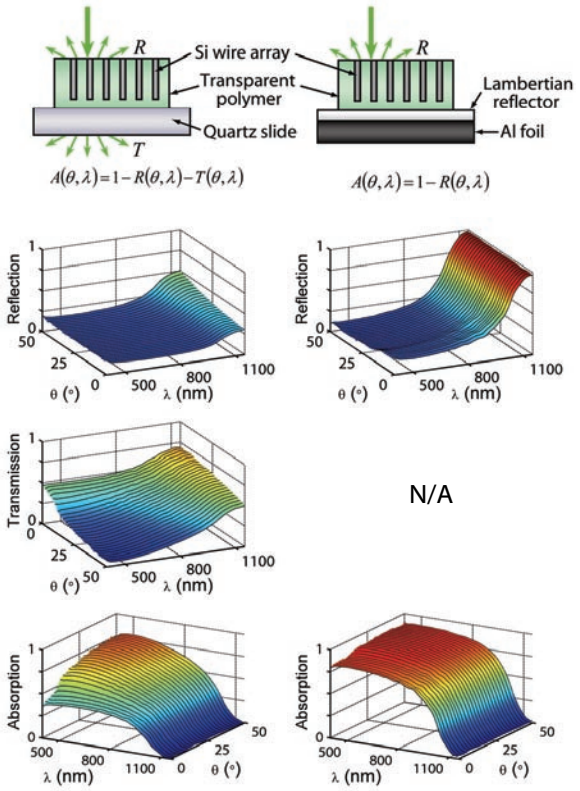

Figure S7. Example absorption measurements. Schematic (top row) and measurements of reflection (second row), transmission (third row), and absorption (bottom row) of a triangular-tiled wire array (η_f = 8.8%), placed on a quartz slide (left column) or a Lambertian back-reflector (right).

array (η_f = 8.8%, 68 μm wire length) are shown in Fig. S7. Similar measurements were performed on all wire arrays in this study.

In Eqns. (1) and (2), θ represents the direction of tilt during measurements, which was usually θ_x as defined in Fig. 1. Due to the angularly anisotropic optical properties of the periodic (e.g. square-tiled) wire arrays (see Fig. 2), it was important that each array be tilted in the same direction with respect to the lattice pattern of the wires—especially when combining angle-resolved reflection and transmission measurements to calculate absorption. Fiducial markings at the corner of each array provided approximate alignment marks; however to ensure reproducible orientation of the periodic arrays within the tilt plane, their transmitted (or reflected) diffraction patterns were used to align

each array's lattice pattern orientation to the match the convention depicted in Fig. 2. Furthermore, the specular reflection from each specimen was used to align the equipment to normal-incidence illumination conditions prior to each measurement.

Sub-bandgap absorption

Spectrally resolved measurements of the wire arrays were also performed at wavelengths exceeding the Si band edge (1150–1200 nm), where no band-to-band absorption is expected. In the absence of a back-reflector, the observed sub-bandgap absorption did not exceed -4% to +12%, and was typically below 5%. Some deviation from zero absorption (negative values in particular) can be attributed to an experimental artifact arising from the spatial variation in the array's optical density, because the transmission and reflection measurements were not necessarily performed at the same location on each wire array specimen. Variations of up to 0.08 in absolute transmission were observed across the wire arrays; however this artifact alone could not account for the larger instances of sub-bandgap absorption, nor that observed when the arrays were placed on the back-reflector (1–16%). Thus, this sub-bandgap absorption may be due to parasitic (non-photovoltaically useful) absorption processes. Parasitic absorption at above-bandgap wavelengths would be detrimental to any photovoltaic device, and must be addressed in this absorption study.

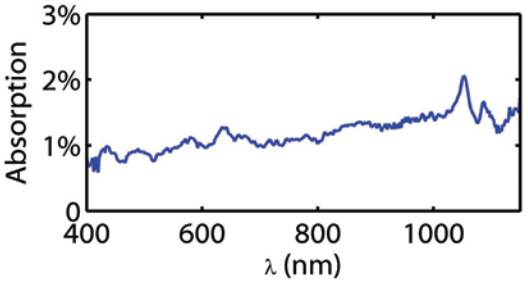

Figure S8. Integrated normal-incidence absorption of ~1-mm-thick PDMS film.

Free-carrier absorption is an intrinsic source of parasitic absorption within Si solar cells.[2] However the absorption due to free-carrier processes was likely negligible at these wavelengths, because most wires were nominally undoped, and the illumination levels were low (<< 1-sun equivalent intensity). Absorption due to the PDMS was also negligible: A relatively thick (est. 1 mm thick) film of cured PDMS exhibited absorption below ~0.02 throughout the measurement range (Fig. S8).

Others have reported sub-bandgap absorption in Au-catalyzed, VLS-grown Si wire arrays (up to ~0.6 at these wavelengths), and this has been primarily attributed to the presence of surface states, defects, or catalyst metal particles[3-5]. It is well-known that certain defects or impurities introduce energy levels or bands within a semiconductor's bandgap, and can give rise to extrinsic (trap-assisted) sub-bandgap absorption.[6] Known as the impurity photovoltaic (IPV) effect, this theoretically useful sub-bandgap absorption mechanism has been proposed and studied as route to exceed the efficiency limit of a single-junction solar cell,[7-9] particularly in non-planar junction geometries.[10-11]

The IPV effect has been experimentally observed at roughened Si surfaces[12] and for Au traps in bulk Si,[13-14] both of which may be present in Au-catalyzed, VLS-grown Si wires. However, IPV absorption has not yet been shown to produce an overall increase in efficiency vs. comparable conventional Si solar cells. Moreover, no sub-bandgap photogeneration has been reported for either surface-state-induced or Au-trap-induced IPV absorption within a purely photovoltaic device. Because of this, and the well-known deleterious properties of surface damage and deep-level traps within Si solar cells, we conclude that IPV absorption, if present, should not presently be considered useful for the purpose of estimating photovoltaic performance limits from absorption measurements.

DOI: 10.1038/NMAT2635

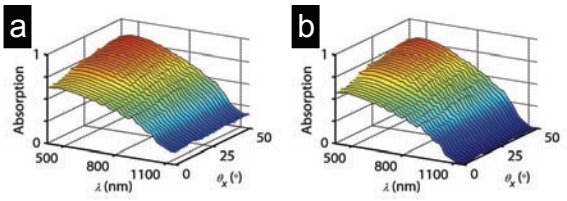

Figure S9. Example of scaling procedure, applied to the measurements of a triangular-tiled wire array (nf = 4.9%) that exhibited ~14% sub-bandgap absorption (placed on a Lambertian back-reflector). **a,** raw absorption data, and **b,** scaled absorption data.

Thus in this study it was assumed that observed sub-bandgap absorption, when present, was parasitic. Parasitic behavior at above-bandgap photon energies could not be determined from the optical measurements, because it cannot be distinguished from Si absorption. If present, however, the above-bandgap parasitic absorption should not be included in the estimation of a solar cell's sunlight utilization potential (A_{avg}), nor should it be included in the comparison of a wire array's absorption to planar absorption limits (as in Fig. 4). Thus to minimize the potential contribution of parasitic absorption to these analyses (as well as to mitigate the experimental artifact described above), the absorption of each wire array was scaled based on its observed sub-bandgap absorption. This was achieved by uniformly scaling (by up to 1.19x) the transmission and reflection measurements of each wire array, so as to produce an absorption (averaged from 1150–1200 nm) equal to that of a PDMS film (~0.01). An example of one of the most extreme cases of this scaling is shown in Fig. S9. Most wire arrays did not require substantial scaling (e.g. Fig 7, in which data appears unscaled.)

Note that the scaling procedure was not applied to the data used to calculate the I.Q.E. of the wire array electrode (Fig. 5), because this experiment sought to investigate parasitic absorption. Furthermore, no scaling was applied to any of the control measurements, or those of non-wire-array absorbers (e.g. the commercial Si solar cell of Figs. 3e and S11). Scaling was also not applied to the photoelectrochemical measurements of external quantum efficiency, since those measurements directly measure useful (non-parasitic) absorption.

It was not clear what caused some samples to exhibit sub-bandgap absorption, while others were virtually transparent at these wavelengths. Because each wire array was subject to identical etching conditions during processing, we suspect that this absorption may be due to entrapped particles of catalyst metal, rather than surface-state or bulk-trap assisted absorption as previously suggested. Catalyst metal inclusions have been observed in Au-catalyzed VLS-grown Si wires,[15] and it is known that Cu and Ni readily precipitate upon rapid cooling within crystalline Si.[16] Unfortunately, the cooling rate of wires following VLS growth varied greatly (and was not controlled) in this study.

Figure of merit calculations

Figure of merit definition

The figure of merit (FOM) utilized in this study calculates the approximate fraction of above-bandgap sunlight (i.e. photocurrent) that a wire array might absorb in a day of operation as a non-tracking solar cell. This calculation combines the angle- and wavelength- dependent absorption measurements $A(\theta,\lambda)$ of each wire array with a standard reference spectrum that specifies the photon flux of direct normal radiation (Γ) at each hour (t) and wavelength (λ) throughout the day[17]. This spectrum represents direct solar insolation typical of a summer day in the southwest U.S. *

Figure S10 depicts the FOM calculation and the associated simplifying conditions. We considered an absorbing device, tilted so as to face the sun at noon, but which did not otherwise track the sun (i.e. oriented at global tilt). The path of the sun across the sky was simplified as an equatorial arc; that is, confined within the equatorial plane such that a single angle $\theta_x(t)$ describes the incidence angle of direct sunlight throughout the day. In this case, $\theta_x = 0°$ at noon and progresses at 15°/hr. Under these assumptions, the fraction of above-bandgap incident photons that would be absorbed from this reference spectrum, A_{avg}, can be expressed as:

$$A_{avg} = \frac{\iint \Gamma(t,\lambda) A(\theta_x(t),\lambda) \cos(\theta_x(t)) \, d\lambda \, dt}{\iint \Gamma(t,\lambda) \cos(\theta_x(t)) \, d\lambda \, dt} \quad (3)$$

This calculation is performed for each wire array, over the range $400 < \lambda < 1100$ nm and $-50° < \theta_x < 50°$ (8:40 to 13:20). These limits are imposed by the spectral range of the illumination source ($\lambda_{min} = 400$ nm) and the Si band edge ($\lambda_{max} \sim 1100$ nm), as well as the mechanical rotation limits of the integrating sphere. This integration range encompasses 255 mAH/cm² of the 305 mAH/cm² of above-bandgap photon-equivalent charge that would strike the global tilt plane under this reference spectrum and associated simplifying assumptions. This calculation (resolved by time of day, t) is plotted as Fig. 3e.

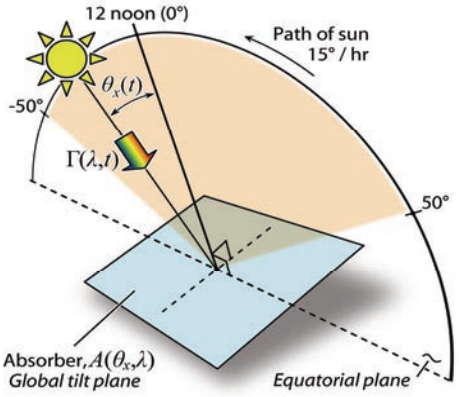

Figure S10. Schematic of FOM calculation

Although this figure of merit calculation effectively utilizes the full extent of the angle- and wavelength-dependent absorption measurements presented herein, it clearly is not a comprehensive model of solar cell efficiency, nor does it attempt to fully approximate realistic solar illumination. One primary limitation is that diffuse, global illumination (which can account for a majority of annual solar irradiation in some areas of the world) is not taken into account. Although a diffuse illumination profile could be broken down by wavelength and incidence angle to assess the absorption of a wire array, diffuse solar irradiation varies greatly by geography, time of day, season, atmospheric conditions, and numerous other factors. This is the subject of much research and modeling, and is beyond the scope of this study. Furthermore, the lack of wire array absorption data corresponding to > 50° incidence angles limits the extent to which the diffuse absorption could be evaluated.

* Note that the reference spectrum was time-shifted to yield maximum direct normal irradiation intensity at noon, to partially correct for differences between solar noon and local time of the reference conditions.

DOI: 10.1038/NMAT2635

In this study, the omission of diffuse irradiation considerations is partially mitigated by the choice of a reference spectrum that is representative of a desert climate. Diffuse irradiation accounts for only ~10% of the total above-bandgap photon current striking the global tilt plane under the reference conditions. Furthermore, since diffuse sunlight strikes a solar cell from all angles, the day-integrated absorption of direct sunlight over ±50°, calculated herein is likely also a reasonable indicator of the wire array's effectiveness at absorbing diffuse sunlight.

Although our figure of merit makes several simplifying assumptions, does not consider diffuse illumination, and neglects additional output efficiency consideration (such as the cell operating voltage) it nevertheless provides an instructive gauge to compare the solar-energy utilization-potential of the wire arrays as a percentage of the theoretical limit of an ideally absorbing Si solar cell. To provide a reference point for this figure of merit calculation, we have also measured the absorption characteristics of a commercial, AR-coated, polycrystalline solar cell using the same integrating sphere apparatus (Fig. S11). This cell's figure of merit (A_{avg} = 0.87) is compared to those of the wire arrays in Fig. 3e.

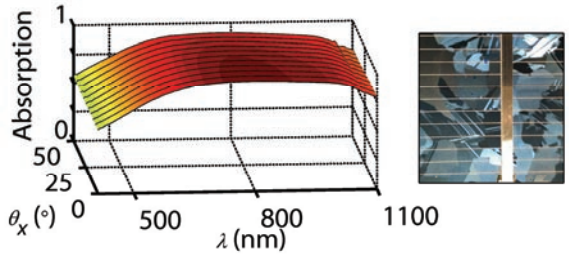

Figure S11. Measured integrated absorption of 280-μm-thick, commercial polycrystalline Si solar cell with dielectric AR-coating. Right: Photograph of ~2 cm square area of this solar cell.

Study of wire array geometry

In this study, 28 unique Si wire arrays were grown by a photolithographically patterned VLS process as previously described.[18] This was achieved using a photomask that included 28 unique hole array patterns derived from seven tiling patterns, with diameters of 3 or 5 μm and minimum pitch (center-to-center distance between adjacent holes) of 7, 9, or 12 μm. The tiling patterns included: periodic (square, triangular); chirped-periodic (square and triangular lattices where each wire had been randomly displaced by up to ±1 μm); quasi-periodic (Penrose, dodecagonal); and quasi-random (random placement of wires not less than the minimum pitch from one another). Wire length was nominally controlled by VLS growth time, however, arrays with higher areal packing fraction exhibited slower growth rates than those with lower packing fractions. In total, wire arrays of each of the 28 unique tiling patterns were grown, with packing fractions ranging from 1.6% to 16%, wire diameters ranging from 1.4 to 4.0 μm, and wire lengths ranging from 24 to 97 μm. The wire array specimens were approximately 5 mm × 5 mm in extent, and had varying optical properties visible to the naked eye (Fig. S12).

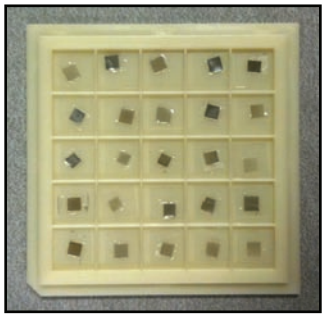

Figure S12. Digital photograph of several wire array samples (in no particular order) illustrating the variation in optical properties visible to the naked eye.

Figures S13a and S13b show the figures of merit for the wire arrays measured in this study, both with (b) and without (a) a Lambertian back-reflector; as a function of areal packing fraction, wire size, and array lattice pattern. The use of a Lambertian back reflector may overestimate the randomization of light that could be achieved by

a metallic back-reflector to a solar cell (which is why the Ag back-reflector used elsewhere in this study, see Figs. 3 and 4). However it was chosen here to approximate the absorption enhancement that was achieved by the use of light-scattering particles (e.g. Al_2O_3) elsewhere in this study, without requiring duplicate arrays to be fabricated with the embedded light-scattering particles.

In general, we found that arrays of moderate (8–10%) packing fraction achieved the highest values of A_{avg}. Although wire arrays with low packing fractions (< 7%) exhibited lower absorption, their A_{avg} values were often many times (10x–25x) their areal packing fractions, with the greatest A_{avg}:η_f ratios corresponding to the longest (up to ~100 μm) wires. This enhancement likely arises from the inherent scattering and diffraction of light along the length of polymer-embedded wire arrays. The wire arrays with the highest packing fractions (12–16%) did not exhibit the greatest absorption, partially because these wires were shorter (~25 μm in length) as a result of a slower VLS growth rate observed for these arrays. Additionally, these dense-packed arrays exhibited greater reflectivity than the moderately packed arrays, presumably due to the increasing surface area of the reflective top surfaces of the wires. Thus, moderate (8–10%) packing fractions with longer (40–60 μm) wire lengths were found to optimize the tradeoff between optical opacity and low reflectivity.

Based on this study, it was determined that reasonable absorption could be obtained with relatively low (< 10%) areal packing fraction of wires. For convenience of growth and characterization, square-packed arrays of relatively long (>60 μm) wires were chosen for further study of optical absorption enhancement, including the use of AR-coatings and light-scattering particles.

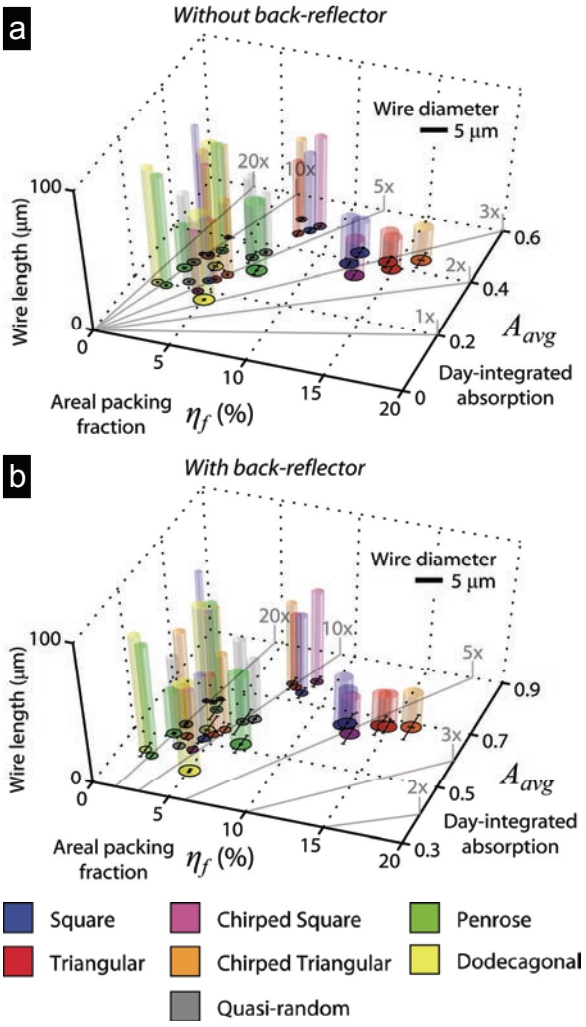

Figure S13. ***A_{avg}*** **values for the wire arrays of this study, a,** measured with no back reflector (quartz slide), and **b,** measured with a Lambertian (Ba_2SO_4) back-reflector. A_{avg} is plotted on the y-axis, as a function of the areal packing fraction, η_f (x-axis), wire length (cylinder height on z-axis), wire diameter (cylinder width vs. scale bar), and array lattice pattern (by color: red, triangular; blue, square; orange, chirped-triangular; purple, chirped-square; green, Penrose; yellow, dodecagonal; gray, quasi-random.) The gray lines indicate A_{avg} : η_f ratios of 1, 2, 3, 5, 10, and 20, as labeled. A_{avg} error bars indicate the extent of any sub-bandgap absorption factor (discussed above); η_f error bars originate from the variance the diameters of the wires in each array.

DOI: 10.1038/NMAT2635

Photoelectrochemical measurements

Photoelectrochemical cell

Figure S14 compares the electrochemical current-density-voltage data for the p-Si wire arrays with that for a photo-inactive conducting glassy carbon electrode. The measurements were performed in the methyl-viologen-containing electrolyte under illumination from an 808-nm laser diode. For the glassy carbon electrode, the onset of reduction current occurs at ~ -0.55 V vs. the Ag|AgCl reference electrode. Under illumination the photocurrent onset for the p-Si wire arrays occurs at a significantly more oxidizing potential, ~ -0.15 vs. Ag|AgCl, implying a photovoltage of ~0.4 V for this particular sample under these test conditions. Spectral response and external quantum efficiency measurements were made between -0.4 to -0.5 V vs. Ag|AgCl. In this potential regime the dark current measured at the glassy carbon electrode was negligible while the photocurrent response from the wire array was relatively flat and scaled linearly with incident light intensity. A detailed account of the energy conversion properties of similar p-Si wire array electrodes is given elsewhere.[19]

E.Q.E. measurements were performed under chopped (f = 30 Hz) illumination using lock-in detection to record the photocurrent from the wire-array electrode (and reject the contribution of dark current) as a function of wavelength.

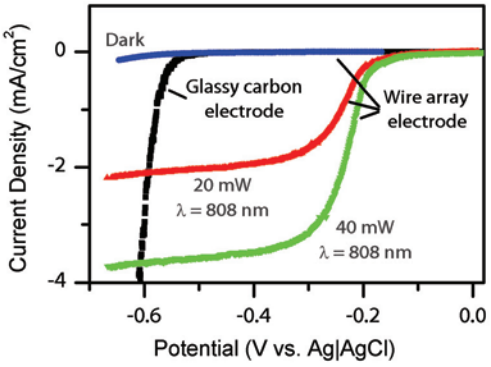

Figure S14. Current-voltage behavior of photo-electrochemical cell

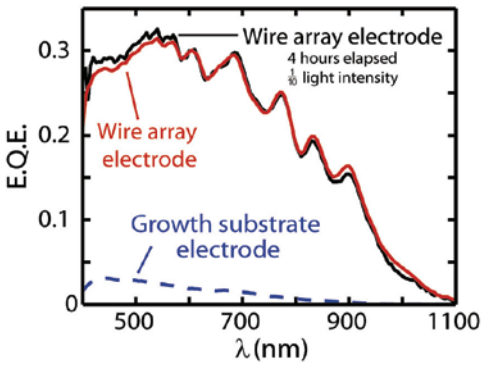

Figure S15. Photoelectrochemical E.Q.E. measurements of the wire-array electrode demonstrating experimental repeatability (red, black). Also shown is the E.Q.E. of the recovered wire-array growth-substrate electrode (blue).

The light source provided relatively low illumination levels (< 10 μA beam photo-current), which avoided mass transport issues within the cell. The E.Q.E. measurements were repeated under varying light intensities and chop rates, over a course of several hours, with negligible difference in the recorded data (Fig. S15). The spectrally-resolved E.Q.E. measurements could be used to predict the J_{SC} of each wire-array electrode by weighting the observed E.Q.E. by the solar spectrum. This was performed to calculate $E.Q.E._{avg}$ (See Fig. S19) .

Determination of I.Q.E.

In this study, the internal quantum efficiency (I.Q.E.) of a radial-junction wire array device was calculated by normalizing the E.Q.E. of a wire array electrode in a photoelectrochemical cell to the optical absorption of a nominally identical, peeled-off wire array. A control electrode was fashioned from the growth substrate of a similarly grown wire array of nearly identical geometry. This wire array had been embedded in PDMS and peeled-off (Fig. 5b, inset right), allowing its optical absorption to be measured. The recovered growth substrate

(Fig. S16, inset) was prepared as an electrode and used for two control experiments.

First, Fig. S15 shows the E.Q.E. of the recovered growth-substrate electrode when measured under identical conditions in the photoelectrochemical cell. The E.Q.E. of the growth substrate was very low (below 0.04) throughout the measurement range, as expected for degenerately doped p^+-Si contaminated with VLS-growth catalyst. The contribution of the growth substrate to the measured E.Q.E. of the wire-array electrodes was likely even less than this, because the wire arrays would partially shade this underlying substrate. Furthermore, a portion of the observed growth-substrate electrode response was likely due to the wire stubs remaining on the growth substrate. Thus, it can be reasonably assumed that the measured E.Q.E. of the wire array electrode corresponds closely to the photoresponse of the wires themselves.

Second, the reflectivity of the recovered growth-substrate was measured (Fig. S16.) The relatively low reflectivity (0.04–0.16) suggests that the growth wafer beneath the wire array electrode did not contribute significantly as an optical back-reflector.

These control experiments validated our approach in approximating the I.Q.E. of the wire array electrode by comparing its E.Q.E. (measured on the growth substrate) to the optical absorption of the identically grown, peeled-off wire array (measured on a quartz slide). Only small differences existed between these experimental configurations. The peeled-off array, embedded in a polymer film of refractive index, $n \approx 1.42$, was placed on a quartz slide (typically exhibiting a reflectivity of ~0.08) for measurement, with a small gap between slide and the array. The wire array electrode, immersed in an electrolyte solution of $n \approx 1.33$ for measurement, remained on its growth substrate with the approximate maximal reflectivity of 0.04–0.15 shown in Fig. S4.

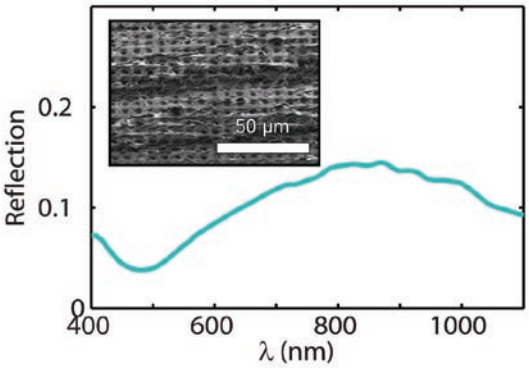

Figure S16. Reflectivity of the growth substrate following peel-off. Inset: SEM image of the recovered growth substrate, remaining wire stubs, and residual PDMS layer (viewed at 45°)

The optical properties of both the wire-array electrode and the peeled-off wire array were highly dependent on the incidence angle of illumination. To assure that the optical and photoelectrochemical measurements were performed at the same illumination incidence angle, θ_x and θ_y were tuned to yield the minimum transmission and E.Q.E., respectively. This corresponded to normal-incidence illumination under both measurement configurations.

At infrared wavelengths (λ > 900 nm), the calculated I.Q.E. deviated from unity, whereas radial-junction theory predicts no such decline for wires of this diameter.[20] We believe that this is likely due to the experimental differences between the absorption and E.Q.E. measurement configurations. Infrared light is weakly absorbed in Si, and thus could be guided to reach the bottom of the wires before being completely absorbed. In the peeled-off configuration, light reaching the bottom of the wires would experience a partial reflection due to the Si/air dielectric interface (~0.32) which could increase absorption. However, light that reaches the bottom of the wires in the electrode configuration would experience no reflection, and would instead be transmitted into (and absorbed within) the thick, photovoltaically inactive growth wafer. This partially explains the drop in inferred I.Q.E. at wavelengths exceeding ~900 nm.

DOI: 10.1038/NMAT2635

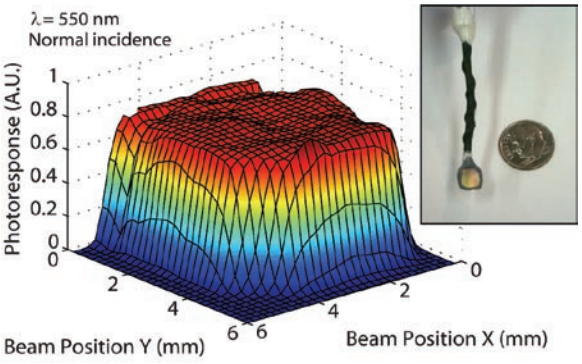

Figure S17. Spatial E.Q.E. uniformity of a wire array electrode. Inset: photograph of wire array electrode.

Supplementary E.Q.E. measurements

Figure S17 demonstrates the spatial uniformity of the E.Q.E. of a Si wire array electrode. In this experiment, the electrode was rastered across a λ = 550 nm beam (approx. spot size of 1 mm²) at normal incidence. No more than ±10% variation in E.Q.E. was observed across the entire device area, indicating excellent uniformity of array geometry and electrical properties.

Figure S18 shows the two-dimensional, angle-resolved E.Q.E. of a square-tiled wire array electrode at λ = 550 nm and λ = 800 nm. The high pattern fidelity of this wire array gave rise to an E.Q.E. profile which was highly dependent on incidence angle. The E.Q.E. was substantially lower at illumination angles parallel to the rows or columns of wires within the array. By convention, most of the absorption/E.Q.E. measurements in this study were performed by varying θ_x with θ_y = 0°, which traverses the

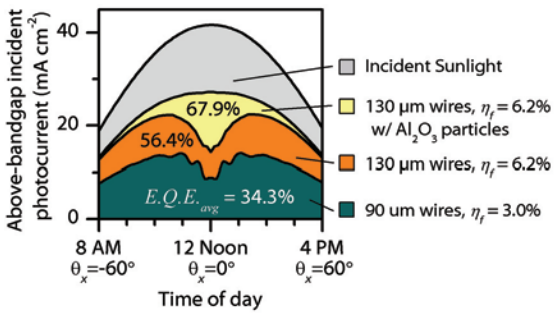

Figure S19. Illustration of *E.Q.E.*$_{avg}$ calculations corresponding to measured wire array electrodes.

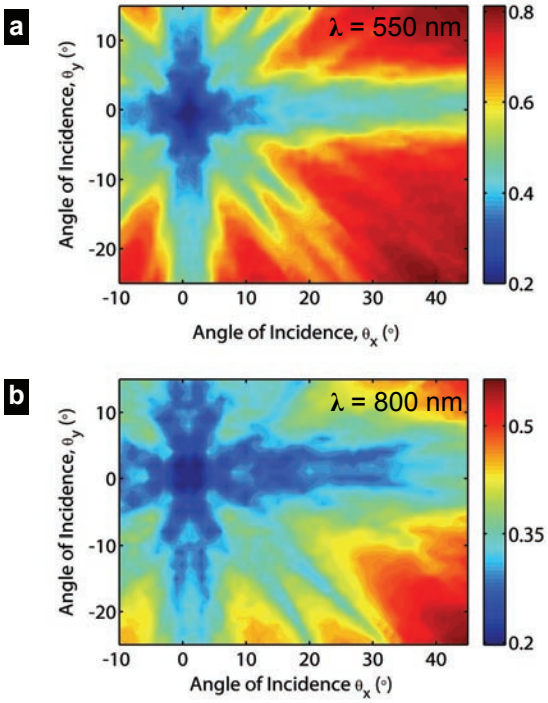

Figure S18. Angle-resolved E.Q.E. of square-tiled wire array electrode, measured at **a,** λ = 550 nm, and **b,** λ = 800 nm.

angles where periodic arrays exhibit minimal absorption/E.Q.E. Thus we note that many of the wire arrays in this study might exhibit increased absorption/E.Q.E. if they were simply oriented differently 8/within the measurement plane. This effect was partially realized by the wire-array electrode of Fig. 5b, which was oriented ~40° compared to the convention followed elsewhere in this study.

E.Q.E. figure of merit

To provide a figure of merit for the E.Q.E. of a wire array electrode, the A_{avg} calculation (defined previously) was performed on the measured E.Q.E. (rather than absorption) of each wire-array electrode, to yield a day-integrated value of external quantum efficiency, *E.Q.E.*$_{avg}$. Fig. S19 illustrates the evaluation of this figure of merit for the wire arrays investigated here. The effectiveness of the Al_2O_3 light-scattering particles can be clearly seen in the improved normal-incidence response of the 130-μm-long wire-array electrode.

References

1 Forouhi, A. R. & Bloomer, I. Optical dispersion relations for amorphous semiconductors and amorphous dielectrics. *Physical Review B* **34**, 7018 (1986).

2 Tiedje, T., Yablonovitch, E., Cody, G. D. & Brooks, B. G. Limiting efficiency of silicon solar-cells. *IEEE Trans. Electron Devices* **31**, 711-716 (1984).

3 Tsakalakos, L. *et al.* Silicon nanowire solar cells. *Appl. Phys. Lett.* **91**, 233117-233113 (2007).

4 Tsakalakos, L. *et al.* Strong broadband optical absorption in silicon nanowire films. *Journal of Nanophotonics* **1**, 013552-013510 (2007).

5 Stelzner, T. *et al.* Silicon nanowire-based solar cells. *Nanotechnology*, 295203 (2008).

6 Pankove, J. I. *Optical processes in semiconductors*. (Prentice-Hall, Inc, 1971).

7 Guttler, G. & Queisser, H. J. Impurity photovoltaic effect in silicon. *Energy Conversion* **10**, 51 (1970).

8 Wolf, M. Limitations and Possibilities for Improvement of Photovoltaic Solar Energy Converters: Part I: Considerations for Earth's Surface Operation. *Proceedings of the IRE* **48**, 1246-1263 (1960).

9 Shockley, W. & Queisser, H. J. Detailed balance limit of efficiency of p-n junction solar cells. *J. Appl. Phys.* **32**, 510-519 (1961).

10 Keevers, M. J. & Green, M. A. in *Photovoltaic Specialists Conference, 1993., Conference Record of the Twenty Third IEEE*. 140-146.

11 Brown, A. S. & Green, M. A. Impurity photovoltaic effect: Fundamental energy conversion efficiency limits. *J. Appl. Phys.* **92**, 1329-1336 (2002).

12 Huang, Z. *et al.* Microstructured silicon photodetector. *Appl. Phys. Lett.* **89**, 033506-033503 (2006).

13 Sah, C. T., Tasch, A. F. & Schroder, D. K. Recombination properties of the gold acceptor level in silicon using the impurity photovoltaic effect. *Phys. Rev. Lett.* **19**, 71 (1967).

14 Guttler, G. & Queisser, H. J. Photovoltaic effect of gold in silicon. *J. Appl. Phys.* **40**, 4994-4995 (1969).

15 Wagner, R. S. Defects in silicon crystals grown by the VLS technique. *J. Appl. Phys.* **38**, 1554-1560 (1967).

16 Seibt, M. & Graff, K. Characterization of haze-forming precipitates in silicon. *J. Appl. Phys.* **63**, 4444-4450 (1988).

17 Marion, B. *et al.* Validation of a photovoltaic module energy ratings procedure at NREL. Report No. NREL/TP-520-26909, (1999).

18 Kayes, B. M. *et al.* Growth of vertically aligned Si wire arrays over large areas (> 1 cm^2) with Au and Cu catalysts. *Appl. Phys. Lett.* **91**, 103110-103113 (2007).

19 Boettcher, S. W. *et al.* Energy-conversion properties of vapor-liquid-solid-grown silicon wire-array photocathodes. *Submitted* (2009).

20 Kelzenberg, M. D., Putnam, M. C., Turner-Evans, D. B., Lewis, N. S. & Atwater, H. A. in *Photovoltaic Specialists Conference, 2009. PVSC '09. 34th IEEE*. 1-6.